International Journal of Nanomedicine

Dovepress
Taylor & Francis Group

Open Access Full Text Article

ORIGINAL RESEARCH

Diselenide-Bridged Iron-Porphyrin MOF for MRI-Guided Radiotherapy via Triple-Pathway Ferroptosis

Wei Huang[1,*], Guangling Zheng[2,*], Banghui Mo[1], Guoqing Jing[2], Mingquan Gao[3], Jinrui Zhao[1], Han Liu[4], Shenglin Luo[3], Songtao Yu[1]

[1]Department of Oncology, Southwest Hospital, Third Military Medical University (Army Medical University), Chongqing, 400038, People's Republic of China; [2]Department of Radiology, Southwest Hospital, Third Military Medical University (Army Medical University), Chongqing, 400038, People's Republic of China; [3]Institute of Combined Injury, Chongqing Engineering Research Center for Nanomedicine, College of Preventive Medicine, Third Military Medical University (Army Medical University), Chongqing, 400038, People's Republic of China; [4]Center of Emergency, Southwest Hospital, Third Military Medical University (Army Medical University), Chongqing, 400038, People's Republic of China

*The authors contribute to this work equally

Correspondence: Songtao Yu, Department of Oncology, Southwest Hospital, Third Military Medical University (Army Medical University), Chongqing, People's Republic of China, Email songtaoyu@tmmu.edu.cn; Han Liu, Center of Emergency, Southwest Hospital, Third Military Medical University (Army Medical University), Chongqing, 400038, People's Republic of China, Email lhmd2009@163.com

Introduction: Radiation resistance poses a significant challenge in clinical cancer therapy. Ferroptosis, an iron-dependent form of cell death, plays an important role in the efficacy of radiotherapy. However, cancer cells often activate defense systems to survive this process. Moreover, interventions targeting only a single defense pathway often yield limited effects.

Methods: To overcome radioresistance, we have developed a reactive oxygen species (ROS)-responsive nanosystem named PRBP. This system employs a siderophore-based framework PCN(Fe) as the core, loaded with two specific drugs: RAS-selective lethal compound 3 (RSL3) to block the glutathione peroxidase 4 (GPX4) pathway, and brequinar (BQR) to inhibit the dihydroorotate dehydrogenase (DHODH) pathway. The surface is coated with a diselenide bond-linked polyethylene glycol (PEG-Se-Se-PEG) layer that dissociates in a ROS-rich environment. Upon X-ray irradiation, the system rapidly degrades and releases the drugs, while iron ions trigger the Fenton reaction. RSL3 and BQR synergistically suppress the ferroptosis defense system, inducing a potent "ferroptosis storm." Through in vitro and in vivo experiments, we systematically evaluated the physical properties, magnetic resonance imaging (MRI) capability, and therapeutic efficacy of this platform.

Results: PRBP exhibits a uniform morphology and undergoes responsive degradation under X-ray irradiation, releasing Fe^{2+} to catalyze the Fenton reaction, leading to DNA damage and glutathione (GSH) depletion. Meanwhile, RSL3 and BQR inhibit the GPX4 and DHODH pathways, respectively, blocking multiple ferroptosis defense targets and thereby inducing robust ferroptosis. PRBP demonstrates favorable T1-weighted magnetic resonance imaging performance, significantly inhibits tumor cell proliferation in vitro, effectively suppresses 4T1 tumor growth in vivo, and exhibits good biosafety.

Conclusion: PRBP induces ferroptosis through multiple targets, providing a potent strategy to overcome radiotherapy resistance.

Keywords: GPX4 inhibitor, DHODH inhibitor, ferroptosis, metal-organic frameworks, radiotherapy

Introduction

Radiotherapy (RT) is one of the key modalities in clinical cancer treatment.[1] High-energy radiation causes DNA damage by ionization, which induces tumor cell death and produces cytotoxic reactive oxygen species (ROS) in a dose-dependent manner for the destruction of cancer cells.[2] However, radioresistance is still one of the most important problems limiting the effectiveness of radiotherapy and restricting its therapeutic options.[3] Recently, there have been reports indicating that a hypoxic tumor microenvironment (TME) and aberrant upregulation of intracellular antioxidant defense systems contribute to the scavenging of RT-induced ROS, which protects tumor

https://doi.org/10.2147/IJN.S610544
Received: 26 March 2026
Accepted: 23 May 2026
Published: 3 June 2026

cells against oxidants and reduces the efficacy of the therapy.[4] Breast cancer is one of the most common malignant tumors among women worldwide.[5] Among its subtypes, triple-negative breast cancer (TNBC) lacks estrogen receptor (ER), progesterone receptor (PR), and Human Epidermal Growth Factor Receptor 2 (HER2) amplification, rendering it inherently resistant to conventional endocrine and targeted therapies and resulting in a poor clinical prognosis.[6] Due to its highly expressed antioxidant defense system, TNBC can resist the increase in reactive oxygen species (ROS) induced by radiation. However, this metabolic reprogramming also leads to an excessive intracellular demand for iron (often referred to as "iron addiction") and an intrinsic vulnerability to lipid peroxidation.[7] Therefore, there is a pressing need to develop novel approaches to circumvent these metabolic barriers and improve the radiosensitivity of TNBC.

Ferroptosis is an iron-dependent, non-apoptotic form of regulated cell death, triggered by the accumulation of lipid peroxidation (LPO). Its morphological characteristics include mitochondrial shrinkage and reduction or disappearance of mitochondrial cristae.[8,9] After a decade of research, ferroptosis has become a major focus of scientific investigation.[10] Owing to its non-apoptotic nature and shared reliance on ROS in RT, ferroptosis has emerged in recent years as a potential breakthrough strategy to overcome radioresistance.[11] Numerous studies have demonstrated an interplay between ferroptosis and radiotherapy: radiotherapy can induce ferroptosis, and ferroptosis, in turn, can enhance the efficacy of radiotherapy.[12] However, owing to robust ferroptosis defense mechanisms in cancer cells, ferroptosis induced by radiotherapy is often insufficient.[13] The cystine/glutamate antiporter (system Xc^-) and glutathione peroxidase 4 (GPX4) constitute the classical defence axis against lipid peroxidation.[14] GPX4 is a specific enzyme that reduces phospholipid hydroperoxide (PL-OOH). Utilizing glutathione (GSH), it converts toxic lipid hydroperoxides into non-toxic lipid alcohols (PL-OH), thereby inhibiting lipid peroxidation.[15] Furthermore, recent studies have shown that dihydroorotate dehydrogenase (DHODH) located in the inner mitochondrial membrane can reduce coenzyme Q (CoQ) to ubiquinol ($CoQH_2$). As a free radical-scavenging antioxidant, $CoQH_2$ prevents lipid peroxidation of the mitochondrial membrane, thereby exerting a ferroptosis-defensive role parallel to that of GPX4.[16] It is particularly noteworthy that, unlike GPX4, which serves as a universal core regulator of ferroptosis, DHODH primarily functions as a parallel defense mechanism within mitochondria. Consequently, interventions targeting a single node often fail due to cellular compensatory mechanisms: if only the cytoplasmic GPX4 pathway is blocked, cancer cells may adaptively rely on the DHODH pathway to evade death; conversely, inhibiting DHODH alone is not a universally applicable ferroptosis inducer, as its efficacy is often limited in certain cell types. To overcome this limitation, we designed the PRBP nanosystem to co-deliver RSL3, BQR, and exogenous iron. By supplementing exogenous iron to promote the Fenton reaction while simultaneously disrupting the two major antioxidant defense axes—the cytoplasmic (GPX4) and mitochondrial (DHODH) pathways—this multi-target strategy effectively overcomes the limitations of single-target inhibition, achieves efficient synergistic induction of ferroptosis, and thereby significantly enhances radiosensitivity.

However, existing small-molecule ferroptosis inducers face multiple challenges such as poor water solubility, low targeting efficiency, and drug resistance, which hinder their clinical application.[17] In recent years, extensive research on nanomaterials has provided new strategies to address these issues.[18] Stimuli-responsive nanomaterials have attracted widespread attention because of their unique spatiotemporal control capabilities.[19,20] Based on this, we designed an X-ray-responsive porphyrinic metal–organic framework (MOF) nanoplatform—PRBP—to achieve synergistic radiotherapy via a triple-pathway ferroptosis amplification mechanism (Scheme 1). Iron-based PCN was selected as the nanocarrier owing to its high porosity for efficient drug loading, inherent radiosensitizing properties of the porphyrin ligand, and ability to supply iron ions as "fuel" for lipid peroxidation.[21] By co-loading the GPX4 inhibitor (RSL3) and the DHODH inhibitor (Brequinar, BQR), a "dual-hit" suppression of the antioxidant system was achieved. Furthermore, the introduction of a diselenium-bond-bridged PEG shell not only ensures circulatory stability but also enables rapid drug release triggered specifically by X-ray irradiation within the tumor microenvironment. Both in vitro and in vivo results demonstrate that PRBP not only serves as a T1-weighted MR imaging agent, but also effectively reverses radioresistance by synchronously inducing iron overload and dual-pathway antioxidant inhibition, thereby triggering a "ferroptosis storm."

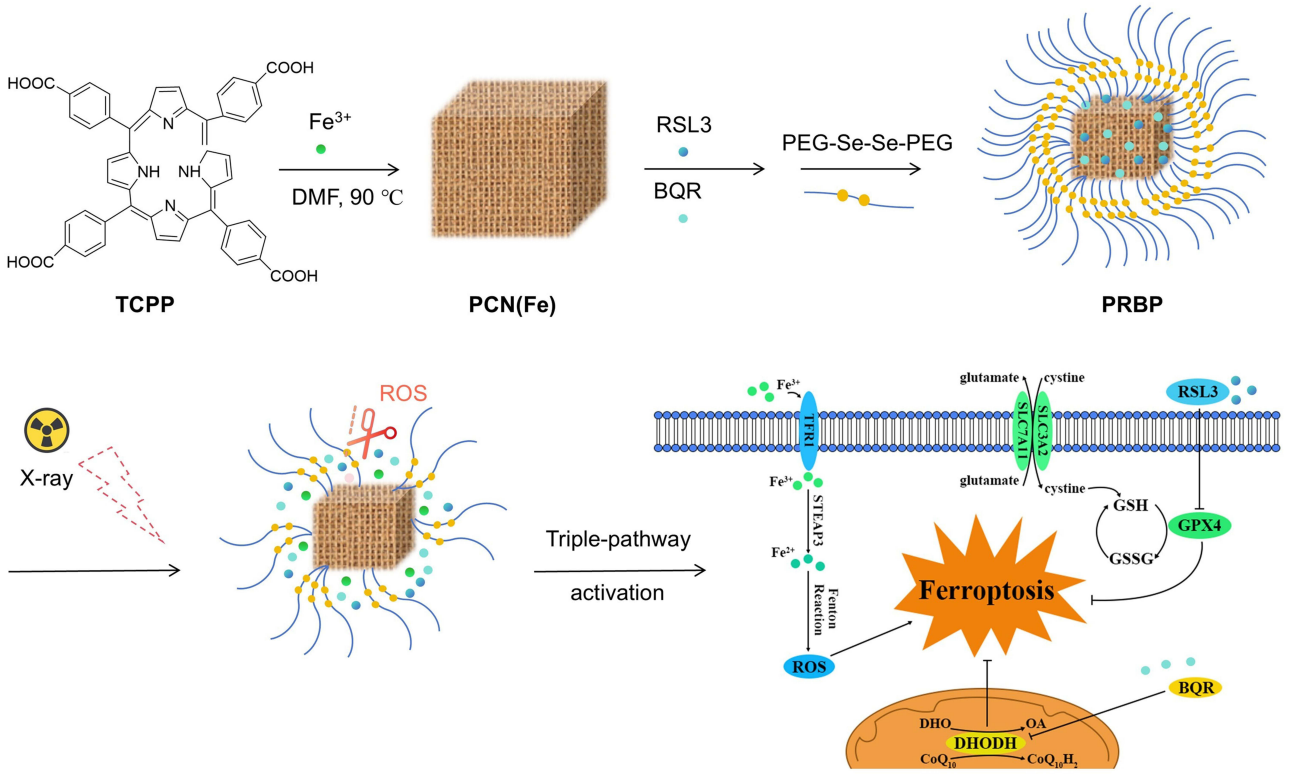

Scheme 1 Preparation of diselenide-bridged iron-porphyrin MOF nanoplatform for radiosensitization by activating triple-pathway ferroptosis. The black flat-headed arrows indicate pathway inhibition, and the red scissors represent the responsive cleavage of chemical bonds.

Materials and Methods

Materials

Iron trichloride hexahydrate (Fe $(Cl_3)_2 \cdot 6H_2O$) was purchased from Energy Chemicals (China). Tetrakis (4-carboxyphenyl) porphyrin (TCPP) was purchased from Solarbio (Beijing, China); RSL3 was bought from Meryer. (Shanghai, China); Brequniar (BQR) was obtained from Shanghai TargetMol, China. Methoxypolyethylene glycols (mPEG; MW:2000) was purchased from Shanghai Adamas, China. 3,3'-Diselenobispropionic acid was purchased from Shanghai Bide Pharmatech Ltd., China.

Characterizations

Transmission electron microscopy (TEM) images were obtained using a FEI TECNAI G2 F20 transmission electron microscope. UV–vis spectra were obtained using an L9 double-beam UV–vis spectrophotometer (Analytical Instrument, Shanghai, China). Powder X-ray diffraction (XRD) analysis was performed using a Thermo escalab 250 XI X-ray diffractometer (USA). Confocal laser scanning microscopy (CLSM) images were recorded on a LEICA TCS SP8 confocal microscope (LEICA, Germany). The high-performance liquid chromatography experiment was completed using the Agilent 1290II from the United States. The ICP-OES data were obtained from the American Agilent ICPOES730.

Synthesis of Diselenide-Modified Polyethylene Glycol (PEG-Se-Se-PEG)

Diselenodipropionic acid (36.5 mg) and DCC (74.3 mg) were placed in a 100 mL round-bottom flask containing 20 mL of DMF. The mixture was stirred in an ice bath at 0 °C for 1 h, followed by the dropwise addition of 3 mg of DMAP dissolved in DMF. Finally, a solution of 0.72 g mPEG-2000 in DMF was slowly added dropwise and the reaction was allowed to proceed overnight. The resulting solution was dialyzed in a dialysis bag for three days and then freeze-dried for two days.

https://doi.org/10.2147/IJN.S610544

Synthesis of PCN(Fe)

$FeCl_3 \cdot 6H_2O$ (10.1 mg), TCPP (4.1 mg), and benzoic acid (112.4 mg) were dissolved in 2.5 mL of DMF in a round-bottom flask and reacted at 90 °C for 5 h under stirring. The product was collected by centrifugation (10,000 rpm, 20 min) and washed with DMF three times. The resulting PCN (Fe) was suspended in DMF and kept away from light.

Synthesis of PRBP, PRP, PBP and PRBP-780

10 mg RSL3, 10 mg BQR, 20 mg Se-PEG(PEG-Se-Se-PEG) and 10 mg PCN (Fe) were dissolved in DMF (5 mL) and stirred overnight at room temperature. Then, the resulting PCN(Fe)@RSL3/BQR-PEG (PRBP) was collected by centrifugation and washed with DMF and water for three times. As controls, PCN(Fe)@RSL3-PEG (PRP) and PCN(Fe)@BQR-PEG (PBP) were synthesized using identical procedures except that only RSL3 or BQR was added to the reaction system. To prepare IR-780-labeled PRBP nanoparticles (PRBP-780), 5 mg of IR-780 dye was added to the reaction system, while the other reaction and purification conditions remained the same.

ROS Responsive Degradation

PRBP NPs were dispersed in H_2O_2 at varying concentrations. After 30 min, partial solutions were extracted for observation by TEM. The reaction progress was confirmed by monitoring the changes in the characteristic absorption bands of the UV–vis spectra using an L9 double-beam.

Hydroxyl Radical (•OH) Generation Experiment

Methylene blue (MB) was used as an indicator to assess •OH generation. A solution containing 60 μM MB and 50 μg/mL of the drug in 1 mL of ultrapure water was incubated. The experimental groups were set as follows: control group (double-distilled water), irradiation group (4 Gy), and irradiation + drug combination treatment group. After treatment, the absorbance of the solution was measured at a wavelength of 664 nm using a microplate reader to evaluate the •OH generation capacity.

Cells and Animals

The 4T1 cells were obtained from ATCC (VA, USA). The 4T1 cells were cultured in Dulbecco's modified Eagle's medium (DMEM) containing 10% fetal bovine serum (FBS; Gibco, USA) and 1% penicillin-streptomycin sulfate (HyClone, USA). All cells were maintained at 37 °C in an incubator with a humidified atmosphere containing 5% CO_2 concentration. Female BALB/c mice (18–22 g) were purchased from Enswell Biotechnology Ltd. (Chongqing, China). All animal experimental procedures in this study were strictly carried out in accordance with the "Guide for the Care and Use of Laboratory Animals" and were approved by the Animal Welfare and Ethics Committee of Army Medical University (Ethics Approval Number: AMUWEC20252120). Mice were housed in standard laboratory animal facilities under a 12-hour light and 12-hour dark cycle, with free access to standard maintenance feed and water. Before the start of the experiment, all mice were acclimated. During subsequent experimental procedures (such as orbital venous blood collection and in vivo imaging, etc.), the animals were anesthetized by inhaling isoflurane. At the end of the experimental period, the mice were euthanized by cervical dislocation after being anesthetized with isoflurane.

In vitro Tumor Cell-Killing Assessment

Cytotoxicity toward 4T1 cells was investigated using the cell counting kit-8 (CCK-8) assay (Beyotime Biotechnology, China). The 4T1 cells were plated in 96-well plates at the cell density of 1×10^4/well and incubated for overnight at 37 °C. The cells were then incubated with different concentrations of PRBP for 6 h, followed by exposed to radiation doses of 0 or 4 Gy (X-ray, 1.04 Gy/min), and further culture for 72 h. The cell survival rate was measured as described in CCK-8 kit instructions. The absorbance was measured at 450 nm using a microplate reader (Thermo Fisher Scientific, USA), and cell viability (%) was calculated by comparing the absorbance with that of untreated cells.

Clone Formation Assay

To test the radiosensitizing effect of PRP, PBP, and PRBP NPs, 4T1cells were plated into 6-well plates and grown overnight in DMEM media and co-cultured with PRP, PBP, and/or PRBP (concentration of 10 μg/mL) for 6 h then exposed to irradiation at 0 or 4 Gy. After irradiation, cells were cultivated for 24 h. Cells subjected to different treatments were reseeded into 6-well plates at a density of 500 cells per well and further cultured under standard conditions for 7 days. After culturing, cells were fixed with paraformaldehyde (4%) and stained with crystal violet (0.1%). The excess dye was washed off in running water, and the plates were left to dry in air at ambient temperature.

In vitro γ-H2AX Foci Staining

Phospho-histone γ-H2AX immunofluorescence staining was used to analyze DNA double-strand breaks. 4T1 cells were seeded in confocal plates and left to adhere overnight. The culture medium was replaced with fresh medium supplemented by PRBP (10 μg/mL). After 6 h of incubation, the cells were irradiated with 0 or 4 Gy and cultivated for three days. The cells were treated with a DNA damage fluorescent probe kit (Beyotime Biotechnology, China) and detected according to the product manual. Fluorescence imaging was performed using a confocal laser scanning microscope (Leica TCS SP8, Leica Microsystems, Germany).

Intracellular ROS Detection

Intracellular ROS generation induced by PRBP NPs was assessed using a Reactive Oxygen Species Assay Kit with the fluorescent probe 2',7'-dichlorofluorescein diacetate (DCFH-DA, Beyotime, China). 4T1 cells were treated with PRBP for 6 h and subsequently exposed to either 0 or 4 Gy irradiation. After 4 h, the culture medium was replaced with DCFH-DA solution and the cells were further incubated for 30 min. Finally, cells were observed under a fluorescence microscope.

Live /Dead Cell Staining Assay

4T1 cells were seeded in 6-well plates at a density of 2×10^5 cells per well and cultured overnight to allow cell attachment. After washing twice with PBS, cells were treated with PBS and 10 μg/mL PRBP for 6 h, followed by irradiation at doses of either 0 or 4 Gy. Following incubation for 72 h, cells were stained with Calcein-AM and PI solutions (DOJINDO, Japan) for 30 min. After washing thrice with PBS, live and dead cells were observed using a fluorescence microscope.

Ferrous Ion Assay

To determine the effect of PRBP on ferrous ion levels in 4T1 cells, a Cellular Red Fluorescent Ferrous Ion Assay Kit with RhoNox-6 (Beyotime, China) was used. 4T1 cells were seeded in 6-well plate, and incubated overnight for cell adhesion. After treatment with PBS or 10 μg/mL PRBP for 6 h, cells were irradiated with 0 Gy or 4 Gy. After another 72 h of culture, cells were washed and then incubated with the prepared RhoNox-6 solution (37 °C) under darkness for 30 min.Staining results were visualized using fluorescence microscope.

Lipid Peroxidation Assay

The 4T1 cells were seeded overnight in confocal dishes prior to treatment. The cells were then treated with PRBP (0 μg/mL) for 6 h, followed by exposure to either 0 Gy or 4 Gy of irradiation. After 72 h of culture, the medium was replaced with fresh medium containing 1 μM Liperfluo solution (DOJINDO, Japan) to assess lipid peroxidation levels. After incubation for 30 min, the cells were washed with PBS and lipid peroxidation levels were analyzed using confocal laser microscopy.

Western Blotting

The cells were treated with PRP, PBP, or PRBP for 6 h, followed by exposure to either 0 or 4 Gy of irradiation. The proteins in these cells were extracted and analyzed by Western blot using primary antibodies against GPX4 (Proteintech, 67763-1-Ig, 1:1000) and β-actin (Proteintech, 81115-1-RR; 1:10000) Following incubation with horseradish peroxidase-

conjugated secondary antibodies for 2 h at room temperature, proteins were visualized by chemiluminescence using an Imaging System.

Bio-TEM Observation of Mitochondrial Morphology

4T1 cells were treated with PRP, PBP, or PRBP for 6 h, followed by exposure to either 0 or 4 Gy of irradiation. Cells were harvested and fixed with 2.5% glutaraldehyde. Subsequently, the cells were sectioned using a slicer to obtain bio-TEM images (FEI Tecnai G2 120KV, USA).

Subcutaneous 4T1 Tumor-Bearing Mice Model and NIR Imaging

The 4T1 cells were suspended and counted in cold PBS, and 1×10^6 4T1 cells were subcutaneously injected into the right back area of the mice. After intravenous injection of 200 μL of 3 mg/mL PRBP-780 via the tail vein into 4T1 tumor-bearing mice, in vivo near-infrared fluorescence imaging was performed 1, 3, 6, 9, 12, 24, 48, 72, and 96 h post-injection. The mice were sacrificed 72 h after administration, and the major organs (heart, liver, spleen, lung, kidney, muscle, and intestine) and tumor tissues were collected for ex vivo imaging. The NIR images were acquired using an Aniview 100 imaging system (BLT, China).

In vitro and in vivo MR Imaging

Magnetic resonance imaging (MRI) studies were conducted on PRBP solutions with various concentrations (2.5–10 mg/mL). For the in vivo imaging experiments, 4T1 tumor-bearing mice were intravenously injected with 200 μL of PRBP solution, and MR images were acquired at different time points using a 1.5 T clinical MRI scanner (Siemens, Germany). The relative T1-MRI signal intensity was quantified using ImageJ software by calculating the tumor-to-muscle (T/M) signal ratio, which was then normalized to the pre-injection baseline (0 h).

In vivo Antitumor Efficacy

Once the average tumor volume reached approximately 200 mm^3, 4T1 tumor-bearing mice were randomly divided into four groups (n=5 per group) and administered normal saline, X-ray, PRBP, or PRBP + X-ray, with the nanoparticle concentration set to 20 mg/kg(based on body weight). Mice that required radiation therapy received a 4 Gy dose of X-ray irradiation 24 h after injection. Tumor size and body weight changes were monitored throughout the experiment, and tumor volume was calculated using the following formula:

$$Volume = \frac{Length \times (Width)^2}{2}$$

At the Day 14th post drug treatment, all mice were euthanized, and subcutaneous tumors were carefully excised and photographed. Tumor tissues and major organs (heart, liver, spleen, lung, kidney) were collected for hematoxylin-eosin (HE) staining. Tumor cell proliferation and apoptosis were assessed using immunofluorescence staining for Ki-67 and TUNEL assays, respectively. The expression levels of GPX4 and DHODH in tumor cells were evaluated by immunofluorescence staining of GPX4 and DHODH.

Biosafety Assessment

To evaluate the potential in vivo toxicity of PRBP, healthy BALB/c mice were administered a single intravenous injection of 10 and 20 mg/kg of PRBP. Euthanasia was performed 30 days after the injection. Blood samples were collected into coagulation tubes for comprehensive biochemical and hematological analyses, and liver function was assessed by measuring serum levels of alanine aminotransferase (ALT), aspartate aminotransferase (AST), and alkaline phosphatase (ALP). Renal function was evaluated based on blood urea nitrogen (UREA) and creatinine (Cr) concentrations, and standard hematological parameters such as white blood cell count (WBC), red blood cell count (RBC), and platelet count (PLT).

Hemolysis Assay

The RBCs isolated from the mice were washed several times with PBS by repeated centrifugation until a clear supernatant was obtained and used in the hemolysis assay as follows: PBS was used as the negative control, and deionized water was used as the positive control. RBCs were incubated with various concentrations of PRBP nanoparticle were co-incubated to RBCs at room temperature (4 h). The mixtures were vortexed and centrifuged (3000 rpm for 10 min). The absorbance of the supernatant was measured at a wavelength of 540 nm. The Hemolysis ratio was computed using the following formula:

$$Hemolysis(\%) = \frac{OD_{sample} - OD_{negative}}{OD_{positive} - OD_{negative}} \times 100\%$$

Statistical Analyses

GraphPad Prism 9.5 were used for data analysis. The data met the assumptions of the statistical tests applied. Student's *t*-test was used for comparison between the two groups, and single factor analysis of variance (ANOVA) was used for multiple groups. Data were showed as mean ± standard deviation (SD). $*p < 0.05$ displayed significant difference and $**p < 0.01$ or $***p < 0.001$ presented extremely significant difference.

Results and Discussion

Preparation and characterizations of the PRBP

First, the PCN(Fe) framework was constructed via employing TCPP and Fe (III) as building blocks using the solvent thermal method.[22,23] Transmission electron microscopy (TEM) images showed a fusiform-like morphology of the PCN(Fe) nanoparticles with a length of approximately 180 ± 20 nm and width of 150 ± 10 nm (Figure 1A and B). Next, through a simple one-pot stirring process, RSL3 and BQR were loaded into PCN(Fe) as porous metal-organic frameworks. Finally, diselenium-bridged PEG (PEG-Se-Se-PEG) was explored for further surface modification to obtain PRBP, with the aim of enhancing stability and realizing ROS responsiveness. TEM images revealed that PRBP maintained a uniform spindle-like morphology with a slight increase in size, approximately 250 ± 20 nm in length and 200 ± 10 nm in width (Figure 1C and D). To confirm the successful synthesis and chemical composition, X-ray photoelectron spectroscopy (XPS) and Fourier transform infrared (FTIR) spectroscopy were employed. The XPS survey spectrum clearly proved the coexistence of C, N, O, Fe, F, and Se in the final complex (Figure 1E). Specifically, the appearance of the Se 1s peak confirms the successful introduction of the diselenide-bridged PEG shell. The FTIR spectra (Figure 1F) consistently exhibited the characteristic peaks of the PCN(Fe) scaffold, RSL3, and BQR, further verifying the successful encapsulation of the therapeutic agents. The optical properties were investigated by UV-vis absorption spectroscopy (Figure 1G), where PRBP retained the characteristic Soret band of the porphyrin structure. Furthermore, the elemental mapping results demonstrated the homogeneous distribution of the expected elements (Fe, F, Se, Cl) (Figure 1H), further supporting that PRBP was successful prepared. According to the High-Performance Liquid Chromatography (HPLC) analysis results, the encapsulation efficiency (EE%) of RSL3 is 70.82%, and its loading efficiency (LE%) is 30.30%. For BQR, the encapsulation efficiency (EE%) is 62.9%, and the loading efficiency (LE %) is 26.91%. Based on the results from inductively coupled plasma optical emission spectrometry (ICP-OES), the iron content of PRBP is approximately 9.39 wt%.

Stimulus-Responsive Degradation and MR Imaging in vitro

To simulate the microenvironment where reactive oxygen species (ROS) levels increase in tumor cells under X-ray irradiation, the response behavior of the PRBP nanomaterial was investigated under varying concentrations of H_2O_2. As the H_2O_2 concentration increased, the absorbance at the characteristic wavelength of PRBP decreased significantly (Figure 2A), indicating structural changes. Further observation by transmission electron microscopy (TEM) revealed partial and obvious structural disintegration of the material under 1 mM and 3 mM H_2O_2 conditions, respectively (Figure 2B), demonstrating that this nanoplatform possessed ROS-triggered degradation properties, enabling controlled

 https://doi.org/10.2147/IJN.S610544

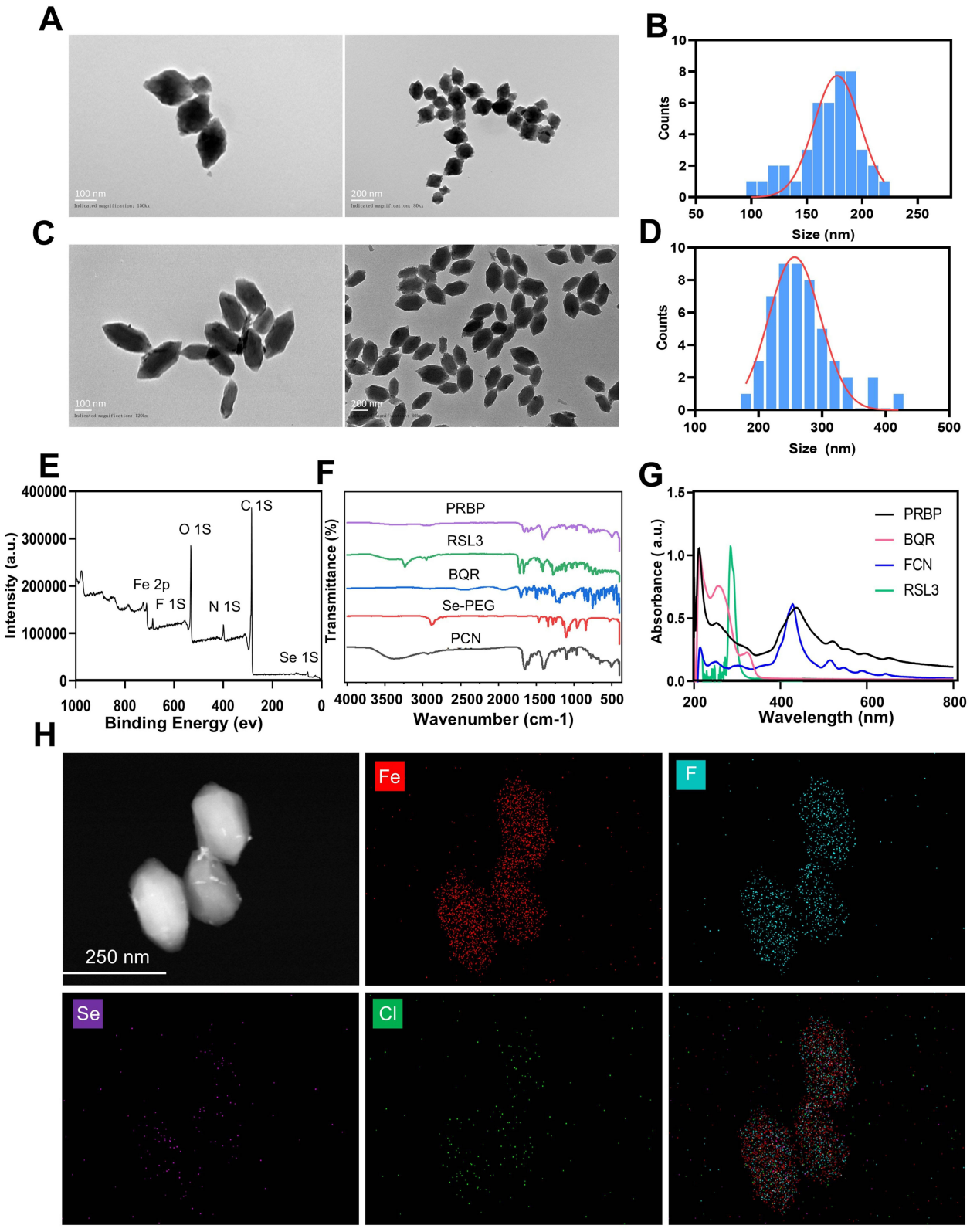

Figure 1 Characterizations of the PRBP. (**A** and **B**) TEM images and size distributions of PCN(Fe). (**C** and **D**) TEM images and size distributions of PRBP (scale bars,100 nm or 200 nm). (**E**) XPS spectra of survey scan for PRBP. (**F**) FTIR of BQR, RSL3, PCN, Se-PEG and PRBP. (**G**) UV–vis spectra of BQR, RSL3, PCN and PRBP. (**H**) TEM-elemental mapping of PRBP.

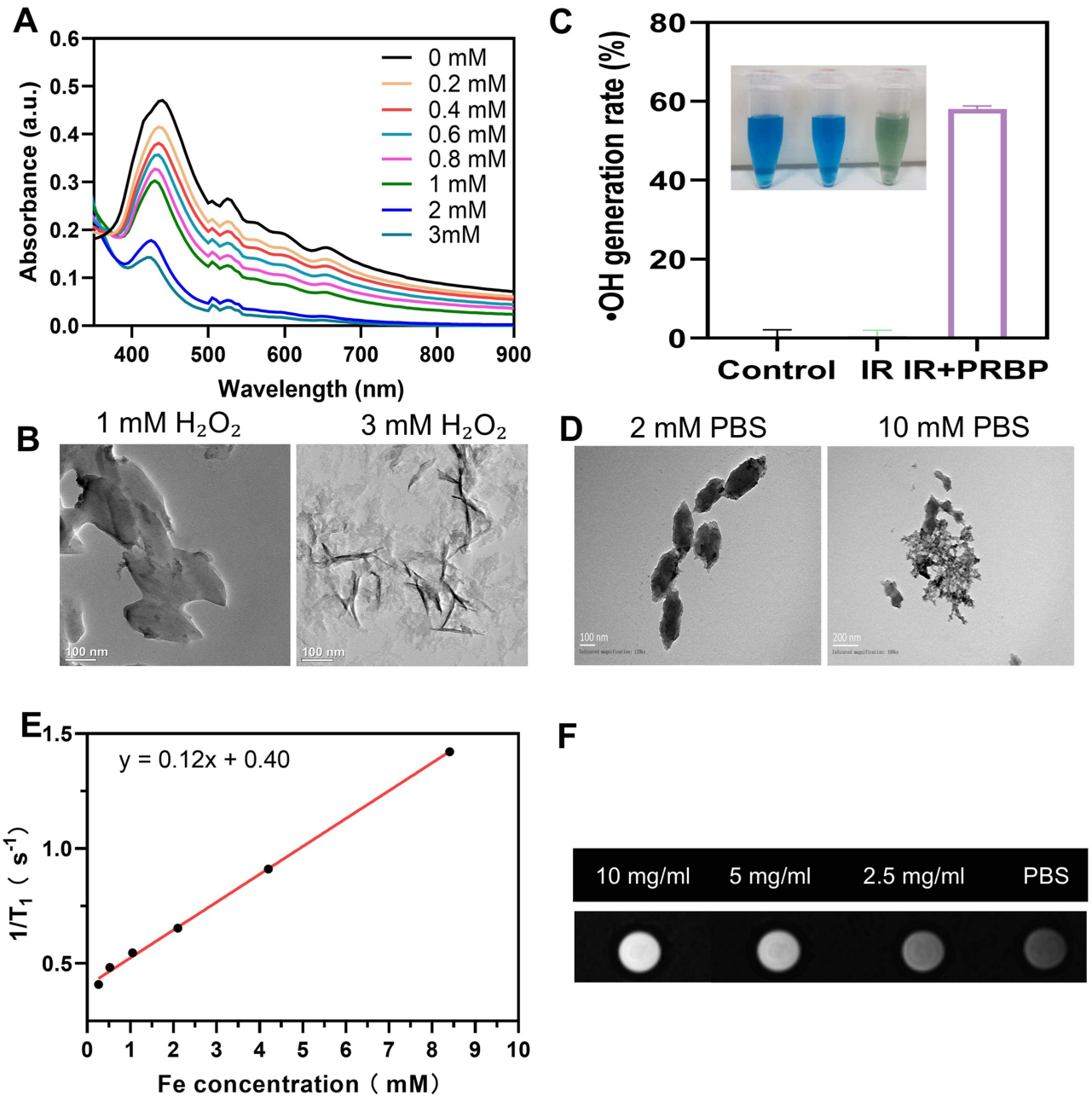

Figure 2 (**A**) UV-vis absorption spectra of PRBP after incubation with varying concentrations of H_2O_2. (**B**) TEM images of PRBP after incubation with 1 mM, and 3 mM H_2O_2 for 0.5 hours. (**C**) Generation of Hydroxyl Radicals under Different Conditions. (**D**)TEM images of PRBP incubated in 2 mM PBS and 10 mM PBS for 4 hours. (**E**) The T1-weighted MR signal intensity of PRBP increased linearly with the Fe (III) concentration (**F**) In vitro T1-weighted MRI using PRBP.

release of the loaded drug. Meanwhile, we evaluated the •OH generation capability of PRBP through a methylene blue (MB) degradation experiment. The results indicate that PRBP exhibits a significant ability to produce ROS under X-ray irradiation (Figure 2C). Additionally, given that the phosphate concentration in cancer cells (approximately 10 mM) is significantly higher than that in extracellular fluid or plasma (approximately 2 mM),[24] the stability of the material was further evaluated under different phosphate concentrations. After incubation in low-concentration PBS (2 mM) mimicking the extracellular environment, the nanoparticles maintained their intact spindle-like morphology. In contrast, after 4 h of incubation in high-concentration PBS (10 mM), simulating the intracellular environment, the material structure showed an obvious collapse (Figure 2D). These results indicated that PRBP remains structurally stable in the bloodstream, effectively preventing premature drug release. After entering tumor cells, its metal-organic framework (MOF)

https://doi.org/10.2147/IJN.S610544

can rapidly dissociate at high phosphate concentrations, thereby accelerating the release of loaded iron ions, BQR, and RSL3.

Meanwhile, the potential of PRBP for magnetic resonance imaging (MRI) ability was confirmed in vitro. Fe (III), as a paramagnetic ion, possesses five unpaired 3d electrons in its outermost shell. It can interact with the protons of water molecules, influencing the relaxation process of the surrounding protons, thereby serving as a contrast agent for T1-weighted MRI. The T1-weighted magnetic resonance signal intensity of PRBP increased linearly with the concentration of nanoparticles (Figure 2E), with an r_1 relaxivity value of 0.12 $mM^{-1}s{-1}$. Concentration-dependent T1-weighted MR images were also obtained (Figure 2F). These results indicate that PRBP has great potential for guiding the in vivo anticancer process.

Amplified Oxidative Stress to Induce Ferroptosis

Cellular uptake of PRBP NPs in 4T1 cells was visually assessed using TEM. As shown in Figure 3A, black dots with a morphology similar to that of PRBP were observed inside the endosome-like vesicles in 4T1 cells by TEM, suggesting that PRBP NPs were taken up through lysosome-dependent endocytosis. Ferrous ion (Fe^{2+})-mediated Fenton reaction is a key process that induces ferroptosis. After entering the cell, the PRBP nanoparticles rapidly disintegrated upon X-ray irradiation and released Fe^{3+} ions, which were subsequently reduced to catalytically active Fe^{2+} by reactive oxygen species (ROS). Figure 3B shows that the strongest intracellular Fe^{2+} fluorescent signals were found in the PRBP + RT group, and the second strongest was observed in the PRBP only treated group, indicating that the tumor microenvironment may participate in and promote the reduction of iron ions. These findings suggest that PRBP in combination with radiotherapy might induce ferroptosis. GSH is an important antioxidant that preserves the cellular redox balance and protects tumor cells against ROS injury, and its high expression has been observed in many tumor cell lines.[25] The intracellular GSH levels were decreased by PRBP treatment (Figure 3C). Accumulation of Fe^{2+} and decrease in GSH, along with the release of the DHODH inhibitor BQR and GPX4 inhibitor RSL3 from PRBP nanoparticles, triggers and amplifies the ferroptosis signaling pathway. The levels of lipid peroxidation were measured to confirm the occurrence of ferroptosis. The results showed that the PRBP + RT group had the highest lipid peroxidation fluorescence intensity (Figure 3D), suggesting that it had the highest capacity to cause damage by lipid peroxidation. To illustrate the synergistic mechanism of these two pathways, the effects of PCN-loaded BQR monotherapy (PBP), PCN-loaded RSL3 monotherapy (PRP), and dual-drug-loaded PRBP on GPX4 expression in 4T1 cells were compared. GPX4 plays an important role in the repair of cell lipid peroxidation, and the inhibition of GPX4 directly induces ferroptosis. As shown in Figure 3E and F, in the absence of radiotherapy, the PRP and PBP monotherapy groups exhibited compensatory upregulation of GPX4 expression, whereas the PRBP group showed a slight decreasing trend. Further comparison between the non-irradiated and irradiated conditions (Figure 3G and H) revealed that the GPX4 expression level in the PRBP treatment group was significantly lower than that in the PRP monotherapy group. Additionally, GPX4 expression in the PRP group was lower than in the PBP group, confirming the effective inhibition of GPX4 by RSL3. These findings suggest that dual-drug combination therapy may effectively block the compensatory mechanisms of cells in response to single-pathway inhibition and that X-ray irradiation can further disrupt the compensatory effects within the cells. Finally, mitochondrial morphology was observed using a bio-transmission electron microscope. We found that the PRBP+RT group exhibited significant mitochondrial atrophy, along with fragmented and reduced mitochondrial cristae (Figure 3I), indicating typical ferroptotic changes in mitochondrial morphology. In this study, we demonstrated that the PRBP nanoplatform coupled with radiotherapy could significantly disturb intracellular redox homeostasis, simultaneously block the two antioxidant systems GPX4 and DHODH, and synergistically amplify lipid peroxidation levels, thereby effectively inducing ferroptosis in tumor cells.

PRBP Enhances Radiosensitivity by Inducing Ferroptosis

To investigate the therapeutic efficacy and radiosensitizing ability of PRBP in vitro, a colony formation assay was first conducted to examine its inhibitory effect on the proliferation of 4T1 cells under X-ray irradiation (Figure 4A). The results demonstrated that the PRBP+RT group exhibited strong tumor growth suppression, whereas the PRP and PBP groups showed effects similar to those of the control group. This phenomenon was considered a result of the dual

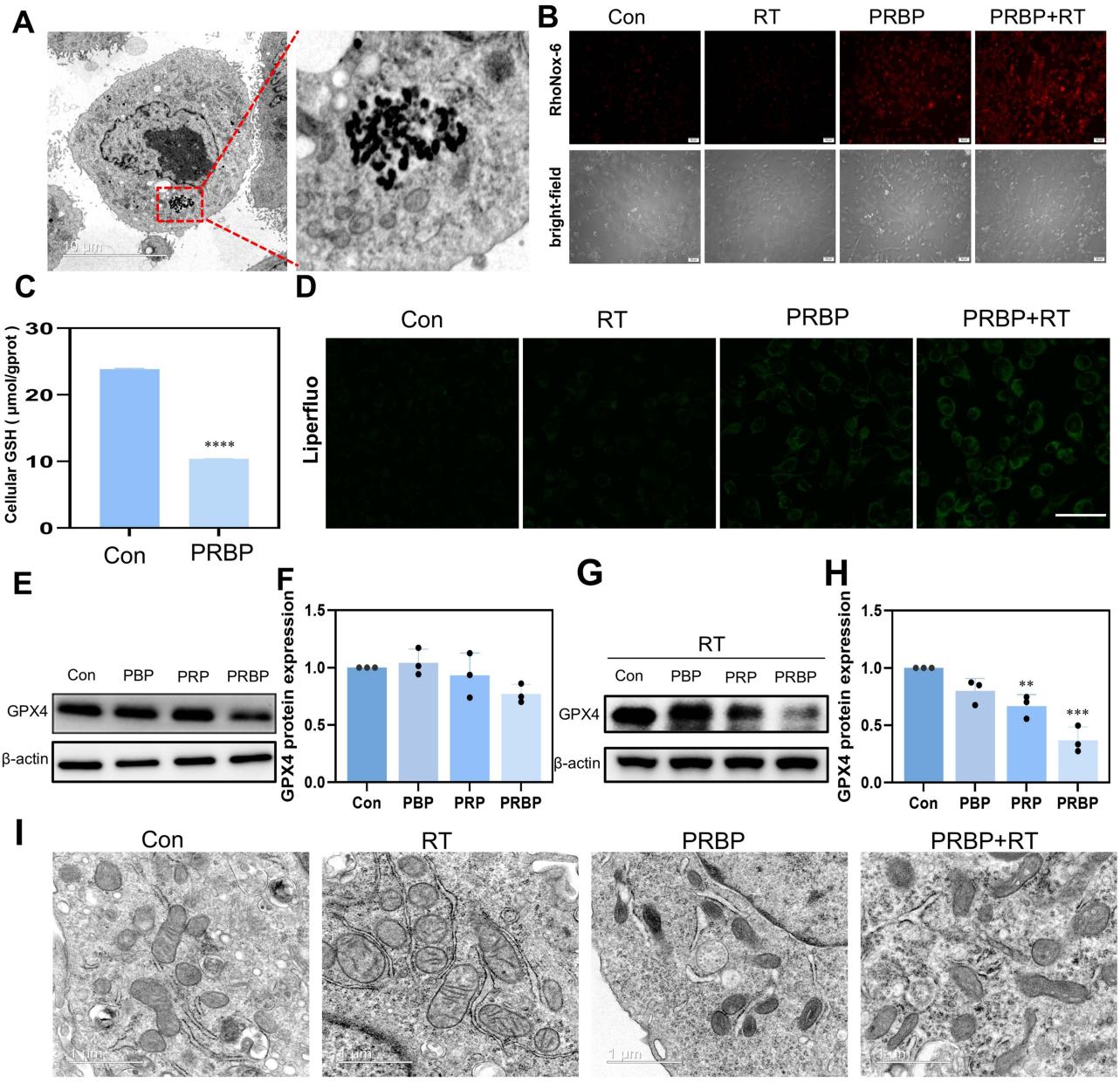

Figure 3 PRBP could act as an efficient ferroptosis inducer. (**A**) Transmission electron microscopy (TEM) images of 4T1 cells incubated with PRBP nanoparticles, revealing abundant nanoparticles localized within lysosomes. (**B**) Fluorescence imaging illustrating intracellular Fe^{2+} levels in 4T1 cells following various treatments. (**C**) Assessment of glutathione (GSH) expression levels in 4T1 cells after drug administration (n = 3, mean ± SD; ****$p < 0.0001$ vs control group). (**D**) Confocal laser scanning microscopy (CLSM) images depicting lipid peroxidation (LPO) in cells subjected to different treatment conditions. Scale bars: 50 μm. (**E–H**) Western blot (WB) analysis of GPX4 expression in 4T1 cells under distinct treatment regimens (n = 3, mean ± SD; **$p < 0.01$, ***$p < 0.001$ vs control group). (**I**) TEM-based observation of mitochondrial morphological alterations in treated 4T1 cells.

suppression of both the DHODH and GPX4 pathways, which enhanced ferroptosis. To validate the radiosensitizing properties of PRBP, a CCK-8 assay was used. As shown in Figure 4B, the PRBP+RT group displayed the most significant cell killing effect. Intracellular ROS generation was detected using DCFH-DA probe. The results demonstrated that the fluorescence of 4T1 cells treated with PRBP alone and irradiation alone was very low; however, cells treated with PRBP + irradiation showed strong green fluorescent signals (Figure 4C), indicating that the Fenton reaction induced by PRBP under irradiation could efficiently produce ROS, which may cause cell DNA damage. Next, DNA damage induced by all these treatments in 4T1 cells was evaluated using a γ-H2AX immunofluorescent stain

https://doi.org/10.2147/IJN.S610544

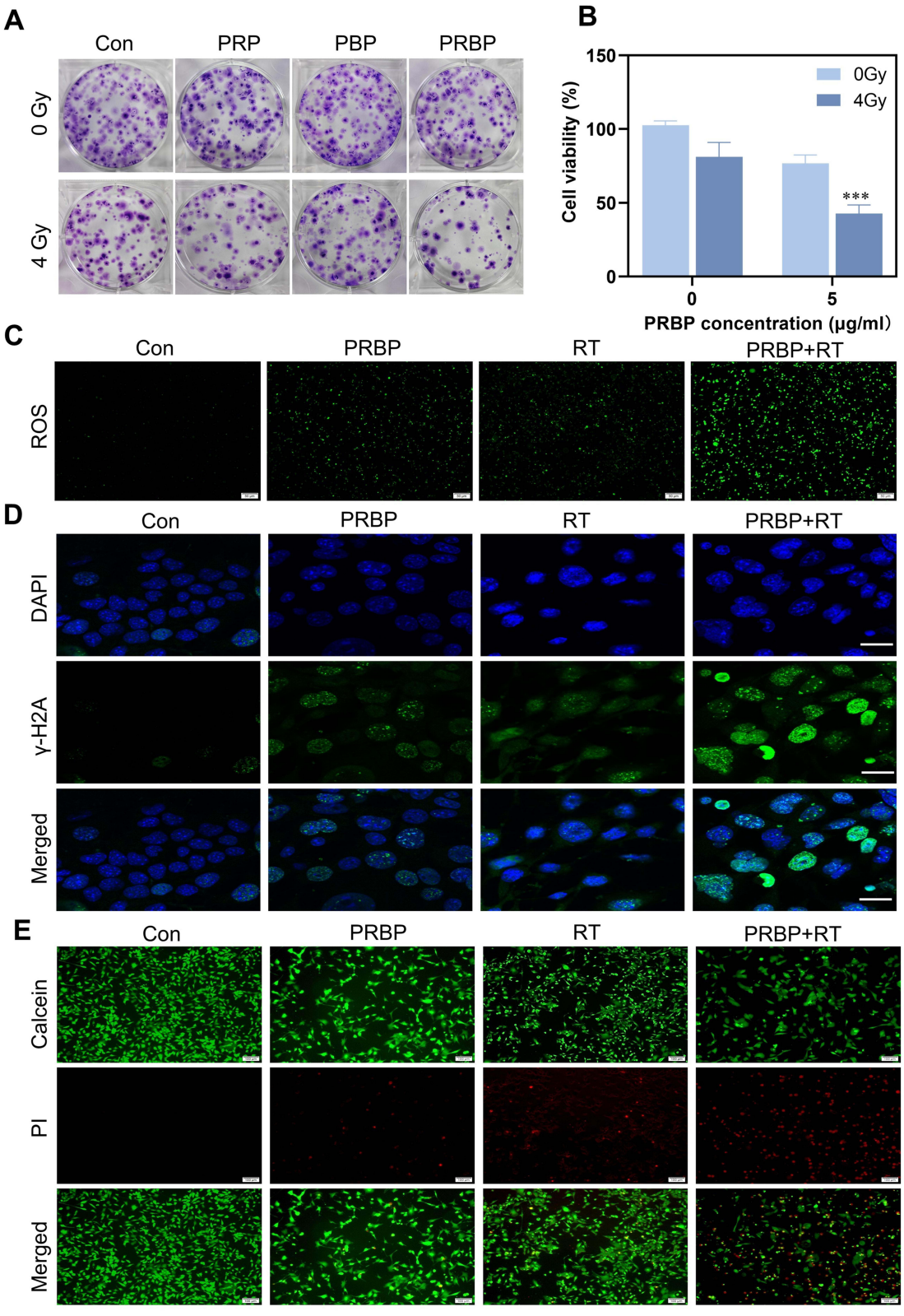

Figure 4 PRBP enhances radiosensitivity by inducing ferroptosis. (**A**) Colony formation images of 4T1 cells treated with PBS, PRP, PBP or PRBP under different X-ray irradiation doses. (**B**) Relative cell viability detected by the CCK-8 assay after treated with PRBP and followed by IR. (n = 3, mean ± SD; ***$p < 0.001$ vs 4 Gy control group). (**C**) Fluorescence images of intracellular ROS levels using DCFH-DA probes. (**D**) Confocal microscopy images of γ-H2AX staining in 4T1 cells subjected to different treatments. Scale bars: 20 μm.(**E**) Live/dead cell staining images of 4T1 cells after different treatments.

https://doi.org/10.2147/IJN.S610544

(Figure 4D), which showed a very low signal for the controls, whereas the RT and PRBP groups displayed weak green fluorescence. Interestingly, the highest number and intensity of γ-H2AX foci were observed in the nuclei of the PRBP + RT group. Our findings indicate that PRBP strongly aggravates DNA damage induced by X-rays, probably because the lack of glutathione and excess lipid peroxides compromise the DNA repair ability of tumor cells, resulting in effective radiosensitization. In addition, the synergistic therapeutic effect of the combined treatment was visually confirmed by Calcein AM/PI double staining (live/dead cell assay) (Figure 4E). The negative control group showed a bright green fluorescent signal (live cells), whereas there was little or no red fluorescent signal (dead cells). The RT and PRBP monotherapy groups showed a moderate increase in red fluorescence, suggesting a degree of necrosis. In sharp contrast, the PRBP+RT group was dominated by intense red fluorescence and decreased cellular populations. The above results also agreed well with those obtained using the CCK-8 assay and provided direct evidence of the powerful cell-killing capability of the combination treatment. In summary, PRBP exhibited considerable radiosensitizing effects.

In vivo Imaging and Biodistribution

Prior to assessing the therapeutic effect of PRBP in vivo, its biodistribution property of PRBP was evaluated in a 4T1 tumor-bearing mouse model. To track the biodistribution of PRBP, a near-infrared fluorescent dye, IR-780, was loaded into PCN along with BQR and RLS3 to obtain PRBP-780. Upon IV injection by the tail vein, a strong IR780 fluorescence signal was detected at the tumor site using an in vivo imaging system. PRBP accumulation at the tumor site was detected at 6 h, whereas the maximal fluorescence signal was observed after 72 h (Figure 5A and C). After 72 h, the mice were sacrificed and the main organs and tumor tissue samples were harvested to detect fluorescent signals (Figure 5B). The results showed that the PRBP mainly concentrations at the tumor site. Specifically, magnetic resonance

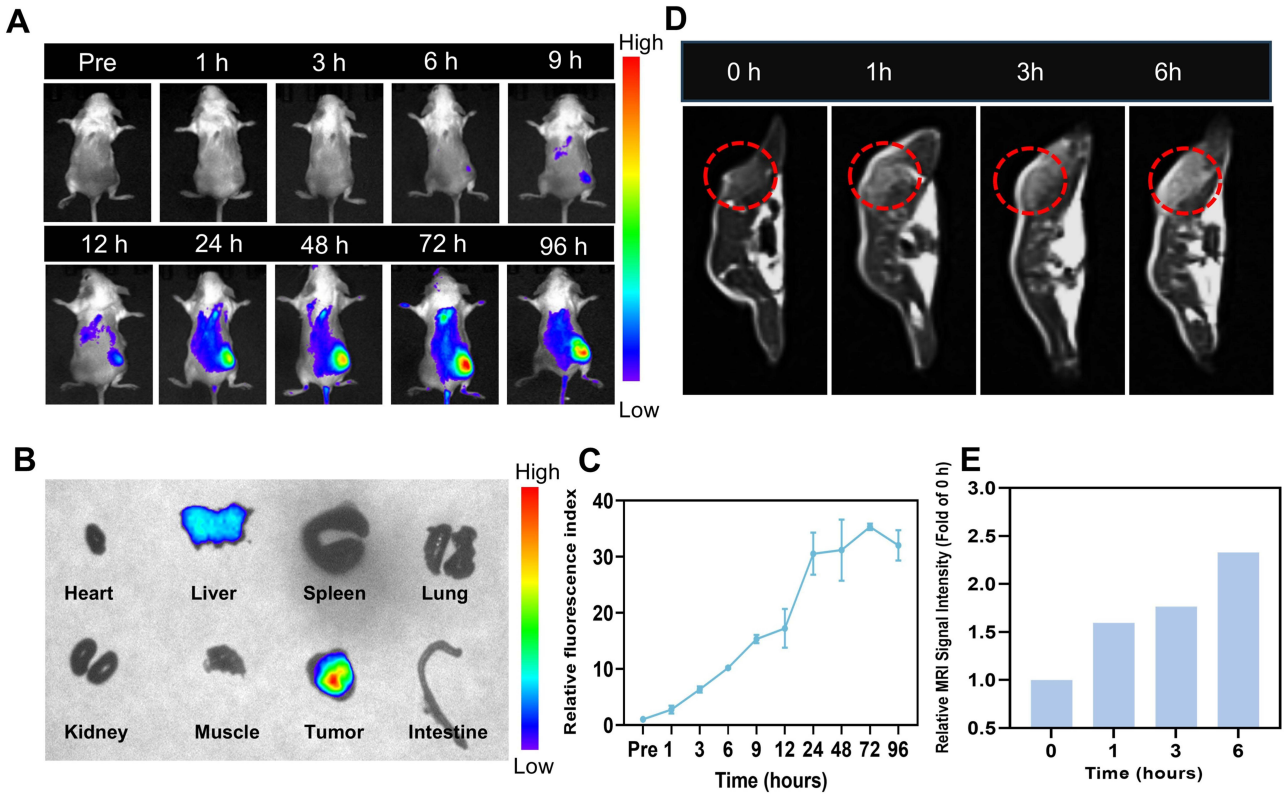

Figure 5 (**A**) Fluorescence imaging of tumor-bearing mice at various time points post-injection of PRBP-780. (**B**) Ex vivo fluorescence images of tumors and major organs at 72 hours post-injection. (**C**) Semiquantitative analysis and comparison of fluorescence intensities (n = 3, mean ± SD). Relative fluorescence index = Fluorescence intensity at time point T / Fluorescence intensity at time point T_0. (**D**) MRI scans of mice at different time points after intravenous injection. The region outlined by the red dashed circle denotes the tumor site. (**E**) Quantitative analysis of T1-weighted MRI signals at the tumor site at 0, 1, 3, and 6 h post-injection.

https://doi.org/10.2147/IJN.S610544

(MR) signals for in vivo imaging and biodistribution at the tumor site were acquired using a 1.5T MRI scanner, as shown in Figure 5D and E. Gradually enhanced bright signals were observed in the transverse section of T1-weighted MR images at the tumor site, indicating that PRBP could accumulate in the tumor tissue via the EPR effect and be used to monitor anticancer progress through dual-mode imaging. In clinical settings, the MR imaging capability of PRBP can be utilized to precisely delineate tumor margins and accurately define radiotherapy target areas, thereby minimizing damage to surrounding healthy tissues. Meanwhile, dynamic MRI monitoring facilitates personalized adjustments to treatment plans and ensures that radiotherapy is triggered when the concentration of local radiosensitizers reaches its peak. Thus, the PRBP platform offers a promising strategy for precision radiochemotherapy.

PRBP Enhanced Radiotherapy Effect in vivo

Based on the aforementioned in vitro efficacy and biodistribution studies, the radiosensitizing effect of PRBP was further validated in vivo. 4T1 tumor-bearing mice were randomly divided into four groups (n=5 per group) and treated as follows: (1) PBS, (2) PRBP, (3) RT, and (4) PRBP + RT. The treatment process is illustrated in Figure 6A. Twenty-four hours after intravenous drug administration, X-ray irradiation was applied locally to the tumor site. During the treatment period, tumor volume and body weight were recorded every three days. As shown in Figure 6B, no significant differences in body weight were observed among the groups, indicating low systemic toxicity of PRBP. The tumor volume curves for various groups are displayed in Figure 6C, where it is clearly demonstrated that tumors in the control group grew rapidly, whereas PRBP + X-ray treatment effectively delayed tumor growth, with a superior therapeutic effect compared with the RT group alone. The tumor images in Figure 6D show that mice treated with PRBP and X-rays exhibited significant tumor growth inhibition mediated by PRBP-induced ferroptosis and RT-induced ROS release, along with the lowest tumor weight (Figure 6E). On Day 14th post drug treatment, H&E staining of tumor tissues (Figure 6F) revealed the highest level of tumor cell death in the PRBP + X-ray group compared to that in the other groups, indicating a significant combinatorial therapeutic effect.

Additionally, immunofluorescence staining was performed for Ki67, TUNEL, GPX4, and DHODH in tumor tissues. As shown, a decrease in red fluorescence (Ki67, a common marker of cell proliferation) and an increase in green fluorescence (TUNEL, a common marker of apoptosis) indicated significant suppression of tumor growth in the PRBP + X-ray group. The Fe^{3+} ions in PRBP induce ferroptosis, whereas released RSL3 inhibits GPX4 expression. X-ray irradiation also altered Gpx4 expression. Under PRBP + X-ray treatment, GPX4 expression was substantially suppressed, effectively triggering ferroptosis in the tumor. BQR inhibited DHODH expression and PRBP + X-ray treatment augmented DHODH inhibition, consistent with our hypothesis. Thus, PRBP + X-ray treatment effectively induced ferroptosis, simultaneously suppressing GPX4 and DHODH and enhancing RT-induced ferroptosis, thereby effectively inhibiting tumor growth.

At the end of the observation period, blood biochemical parameters were measured to conduct a preliminary biosafety evaluation of PRBP. All treatment groups showed fluctuations within the normal range but exhibited no significant differences (Figure 7A and B). After treating red blood cells with different concentrations of PRBP, no hemolysis was observed (Figure 7C). Following treatment, the major organs (heart, liver, spleen, lungs, and kidneys) of the mice from each group were collected for H&E staining. No significant differences were observed between the treatment and control groups (Figure 7D). These results preliminarily confirm the excellent short-term in vivo safety of the nanoplatform. Furthermore, from the perspective of long-term safety, the ability of the reticuloendothelial system (RES) to metabolize and clear nanoparticles over the long term is a critical factor determining their potential for clinical translation. Notably, the core structure of PRBP contains iron porphyrin, which structurally mimics endogenous heme, thereby endowing this nanoplatform with inherent biodegradability.[26] After being phagocytosed by the RES, the iron porphyrin component is expected to be naturally degraded by intracellular heme oxygenase-1 (HO-1) and ultimately safely metabolized or excreted from the body. Therefore, PRBP is highly unlikely to cause long-term accumulation or chronic toxicity in the RES. In summary, PRBP combined with X-ray treatment effectively inhibited tumor growth with favorable biosafety.

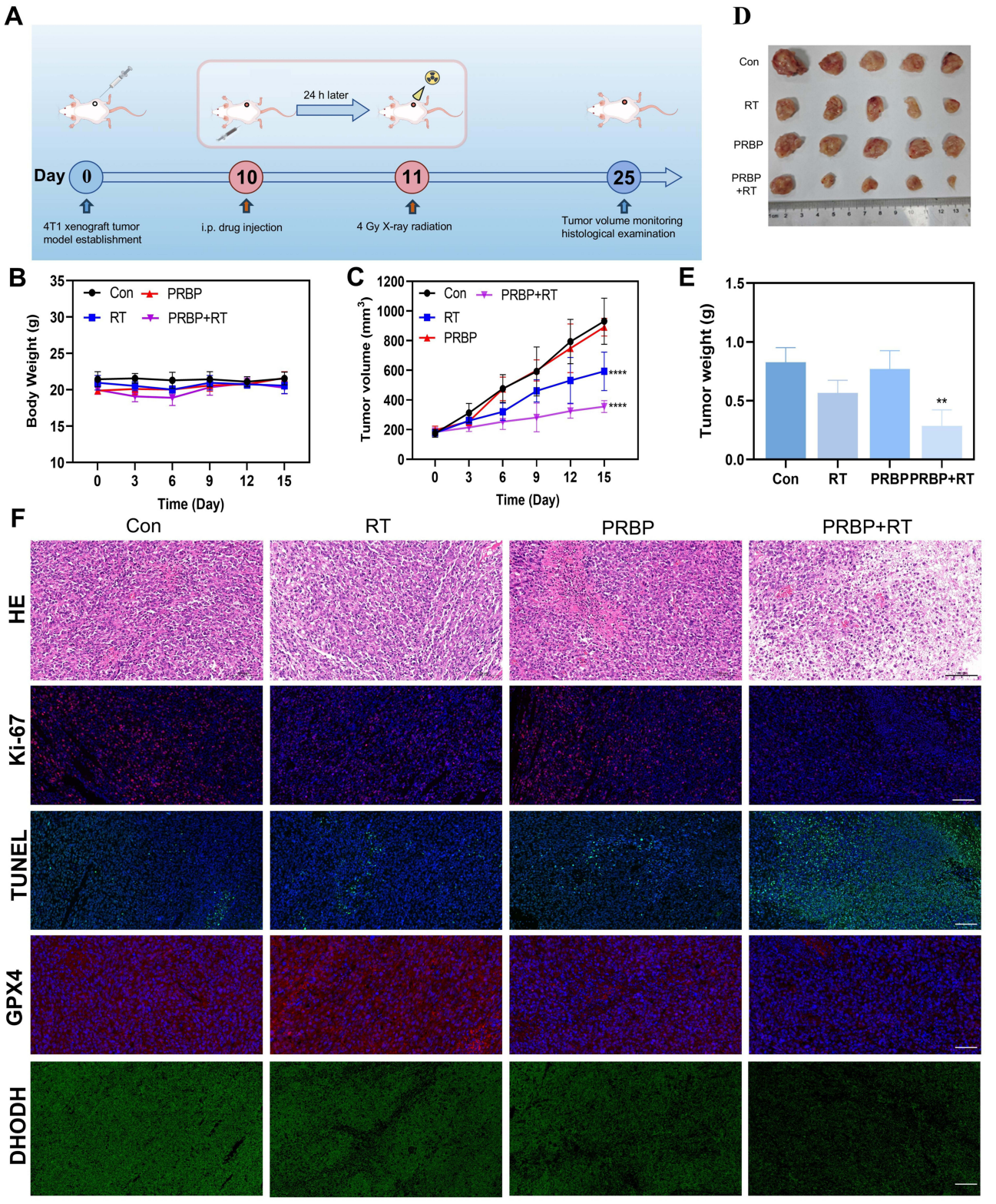

Figure 6 In vivo antitumor efficacy of PRBP. (**A**) Schematic illustrating the treatment schedule administered to 4T1 tumor-bearing mice. (**B**) Body weight changes in mice across different treatment groups (n = 5). (**C**) Tumor growth curves following the indicated treatments. (**D**) Representative photographs of excised tumors from each treatment group (n = 5, mean ± SD; ****$p < 0.0001$ vs control group). (**E**) Tumor weights measured after the respective treatments (n = 3, mean ± SD; **$p < 0.01$ vs control group). (**F**) Histological and immunofluorescence analysis of tumor sections post-treatment: hematoxylin and eosin (H&E) staining; immunofluorescence staining for Ki-67, TUNEL, GPX4, and DHODH. Scale bars: 50 μm.

https://doi.org/10.2147/IJN.S610544

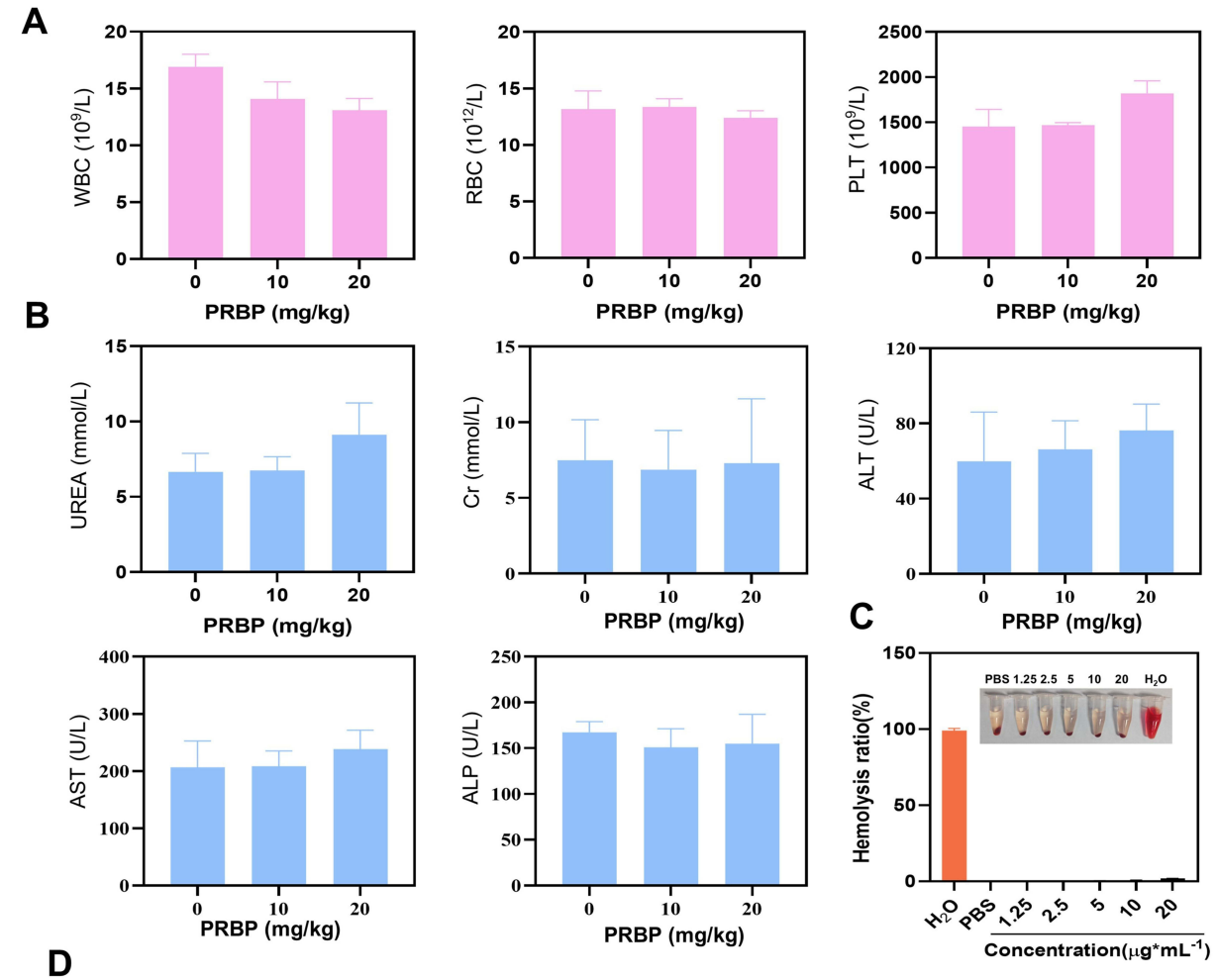

Figure 7 Biosafety evaluation of PRBP. (**A**) WBC, RBC, PLT after different treatments (n = 3, mean ± SD). (**B**) UREA, Cr, ALT, AST, ALP after various treatment (n = 3, mean ± SD). (**C**) Hemolysis rate of red blood cells incubated with different concentrations of PRBP for 3 hours (n = 4, mean ± SD). (**D**) H&E staining images of the heart, liver, spleen, lung, and kidney after different treatments.

https://doi.org/10.2147/IJN.S610544

Conclusions

In summary, this study successfully developed a nanodrug named PRBP based on a metal-organic framework (MOF), which achieved triple synergistic therapy combining radiosensitization and dual-pathway inhibition of GPX4/DHODH for the first time. Under X-ray irradiation, the ROS-sensitive diselenide bonds break, controlling the release of iron ions from PRBP as a catalytic source for the Fenton reaction, while simultaneously releasing RSL3 and BQR. RSL3 inhibits GPX4 activity to block the GSH-dependent lipid repair system, whereas BQR targets the mitochondrial DHODH pathway to suppress the ubiquinone-based antioxidant defense. Additionally, the iron-based MOF core integrated into PRBP endows it with T1-weighted MR imaging capability, enabling real-time tracking of nanodrug distribution and metabolic behavior in vivo, thus offering the potential for image-guided precision radiotherapy. Therefore, our study not only provides an intelligent nanoplatform for overcoming tumor radiotherapy resistance, but also represents a novel strategy for the synergistic development of multifunctional theranostic agents for tumor imaging and therapy.

Funding

This work was supported by the National Natural Science Foundation of China (No.82472972) and the Science and Chongqing Science and Health Joint Medical Research Project (N0.2025ZDXM012).

Disclosure

The authors declare that they have no known competing financial interests or personal relationships that could influence the work reported in this study.

References

1. He MY, Rancoule C, Rehailia-Blanchard A, et al. Radiotherapy in triple-negative breast cancer: current situation and upcoming strategies. *Crit Rev Oncol Hematol*. 2018;131:96–101. doi:10.1016/j.critrevonc.2018.09.004
2. Srinivas US, Tan BWQ, Vellayappan BA, Jeyasekharan AD. ROS and the DNA damage response in cancer. *Redox Biol*. 2019;25:101084. doi:10.1016/j.redox.2018.101084
3. Canha-Borges A, Nunes B, Quintas ST, et al. Emerging mechanisms of triple-negative breast cancer radioresistance: interplay between cancer cell mechanisms and the tumor immune microenvironment. *Cancer Treat Rev*. 2025;140:103026. doi:10.1016/j.ctrv.2025.103026
4. Wang Y, Liu Z, Lv Y, Long J, Lu Y, Huang P. Mechanisms of radioresistance and radiosensitization strategies for Triple Negative Breast Cancer. *Transl Oncol*. 2025;55:102351. doi:10.1016/j.tranon.2025.102351
5. Barzaman K, Karami J, Zarei Z, et al. Breast cancer: biology, biomarkers, and treatments. *Int Immunopharmacol*. 2020;84:106535. doi:10.1016/j.intimp.2020.106535
6. Zagami P, Carey LA. Triple negative breast cancer: pitfalls and progress. *NPJ Breast Cancer*. 2022;8(1):95. doi:10.1038/s41523-022-00468-0
7. Yang F, Xiao Y, Ding JH, et al. Ferroptosis heterogeneity in triple-negative breast cancer reveals an innovative immunotherapy combination strategy. *Cell Metab*. 2023;35(1):84–100.e108. doi:10.1016/j.cmet.2022.09.021
8. Dixon SJ, Olzmann JA. The cell biology of ferroptosis. *Nat Rev Mol Cell Biol*. 2024;25(6):424–442. doi:10.1038/s41580-024-00703-5
9. Mou Y, Wang J, Wu J, et al. Ferroptosis, a new form of cell death: opportunities and challenges in cancer. *J Hematol Oncol*. 2019;12(1):34. doi:10.1186/s13045-019-0720-y
10. Stockwell BR. Ferroptosis turns 10: emerging mechanisms, physiological functions, and therapeutic applications. *Cell*. 2022;185(14):2401–2421. doi:10.1016/j.cell.2022.06.003
11. Pearson AN, Carmicheal J, Jiang L, Lei YL, Green MD. Contribution of lipid oxidation and ferroptosis to radiotherapy efficacy. *Int J Mol Sci*. 2021;22(22):12603. doi:10.3390/ijms222212603
12. Lei G, Mao C, Yan Y, Zhuang L, Gan B. Ferroptosis, radiotherapy, and combination therapeutic strategies. *Protein Cell*. 2021;12(11):836–857. doi:10.1007/s13238-021-00841-y
13. Liu J, Kang R, Tang D. Signaling pathways and defense mechanisms of ferroptosis. *Febs J*. 2022;289(22):7038–7050. doi:10.1111/febs.16059
14. Zhang W, Liu Y, Liao Y, Zhu C, Zou Z. GPX4, ferroptosis, and diseases. *Biomed Pharmacother*. 2024;174:116512. doi:10.1016/j.biopha.2024.116512
15. Xie Y, Kang R, Klionsky DJ, Tang D. GPX4 in cell death, autophagy, and disease. *Autophagy*. 2023;19(10):2621–2638. doi:10.1080/15548627.2023.2218764
16. Mao C, Liu X, Zhang Y, et al. DHODH-mediated ferroptosis defence is a targetable vulnerability in cancer. *Nature*. 2021;593(7860):586–590. doi:10.1038/s41586-021-03539-7
17. Liang C, Zhang X, Yang M, Dong X. Recent progress in ferroptosis inducers for cancer therapy. *Adv Mater*. 2019;31(51):e1904197. doi:10.1002/adma.201904197
18. Lei H, Pei Z, Jiang C, Cheng L. Recent progress of metal-based nanomaterials with anti-tumor biological effects for enhanced cancer therapy. *Exploration*. 2023;3(5):20220001. doi:10.1002/EXP.20220001
19. Li C, Wu X, Zheng C, et al. Nanotechnology-integrated ferroptosis inducers: a sharp sword against tumor drug resistance. *J Mater Chem B*. 2022;10(38):7671–7693. doi:10.1039/D2TB01350A

20. Bai X, Kang J, Wei S, et al. A pH responsive nanocomposite for combination sonodynamic-immunotherapy with ferroptosis and calcium ion overload via SLC7A11/ACSL4/LPCAT3 pathway. *Exploration*. 2025;5(1):20240002. doi:10.1002/EXP.20240002
21. Wang B, Dai Y, Kong Y, et al. Tumor Microenvironment-Responsive Fe(III)-Porphyrin nanotheranostics for tumor imaging and targeted chemodynamic-photodynamic therapy. *ACS Appl Mater Interfaces*. 2020;12(48):53634–53645. doi:10.1021/acsami.0c14046
22. Zhang T, Jiang Z, Chen L, et al. PCN-Fe(III)-PTX nanoparticles for MRI guided high efficiency chemo-photodynamic therapy in pancreatic cancer through alleviating tumor hypoxia. *Nano Res*. 2020;13(1):273–281. doi:10.1007/s12274-019-2610-6
23. Hu X, Li R, Wu W, et al. A Fe(III)-porphyrin-oxaliplatin(IV) nanoplatform for enhanced ferroptosis and combined therapy. *J Control Release*. 2022;348:660–671. doi:10.1016/j.jconrel.2022.06.019
24. Ding Y, Xu H, Xu C, et al. A nanomedicine fabricated from gold nanoparticles-decorated metal-organic framework for cascade chemo/chemodynamic cancer therapy. *Adv Sci*. 2020;7(17):2001060. doi:10.1002/advs.202001060
25. Ursini F, Maiorino M. Lipid peroxidation and ferroptosis: the role of GSH and GPx4. *Free Radic Biol Med*. 2020;152:175–185. doi:10.1016/j.freeradbiomed.2020.02.027
26. Wei YJ, Li J, Hu ZE, et al. A porphyrin-MOF-based integrated nanozyme system for catalytic cascades and light-enhanced synergistic amplification of cellular oxidative stress. *J Mater Chem B*. 2023;11(28):6581–6594. doi:10.1039/D3TB00681F